




High-speed fixed-target serial virus crystallography

Philip Roedig^{1,11}, Helen M Ginn^{2,3,11}, Tim Pakendorf¹, Geoff Sutton², Karl Harlos², Thomas S Walter², Jan Meyer¹, Pontus Fischer¹, Ramona Duman³, Ismo Vartiainen⁴, Bernd Reime¹, Martin Warmer¹, Aaron S Brewster⁵, Iris D Young⁵ , Tara Michels-Clark⁵, Nicholas K Sauter⁵, Abhay Kotecha², James Kelly^{6,7}, David J Rowlands⁶, Marcin Sikorsky⁸, Silke Nelson⁸, Daniel S Damiani⁸, Roberto Alonso-Mori⁸ , Jingshan Ren², Elizabeth E Fry², Christian David⁹, David I Stuart^{2,3} , Armin Wagner³ & Alke Meents^{1,10}

We report a method for serial X-ray crystallography at X-ray free-electron lasers (XFELs), which allows for full use of the current 120-Hz repetition rate of the Linear Coherent Light Source (LCLS). Using a micropatterned silicon chip in combination with the high-speed Roadrunner goniometer for sample delivery, we were able to determine the crystal structures of the picornavirus bovine enterovirus 2 (BEV2) and the cytoplasmic polyhedrosis virus type 18 polyhedrin, with total data collection times of less than 14 and 10 min, respectively. Our method requires only micrograms of sample and should therefore broaden the applicability of serial femtosecond crystallography to challenging projects for which only limited sample amounts are available. By synchronizing the sample exchange to the XFEL repetition rate, our method allows for most efficient use of the limited beam time available at XFELs and should enable a substantial increase in sample throughput at these facilities.

X-ray crystallography has been the dominant method for the determination of high-resolution virus structures in the past 30 years, although electron microscopy plays an increasing role. For nonenveloped viruses, numerous X-ray crystallographic structures have been solved, at resolutions of up to 1.4 Å (ref. 1). Owing to the large unit cell and limited sizes of the crystals, Bragg reflections from virus crystals are typically weak^{2,3}. Thus, X-ray structure determination of virus crystals is ideally carried out at highly brilliant X-ray sources, thus allowing a large number of photons to be focused into a small spot ideally matching the size of the virus crystals⁴. A further challenge is radiation damage. Structure determination from biological macromolecules is usually carried out at cryogenic temperatures to decrease the detrimental effect of ionizing radiation on crystal diffraction^{5–7}. Although finding appropriate conditions for cryoprotection is often straightforward for many protein crystals, doing so has remained a challenge for

virus crystals, because they possess only weak crystal contacts, and a small increase in crystal mosaicity often results in overlapping reflections and a decrease in the measured resolution^{2,3}. Thus, to date, relatively few virus structures have been determined at cryogenic temperatures¹, and most work is performed at room temperature⁴.

A promising method for biological structure determination from virus crystals is serial femtosecond X-ray crystallography (SFX)^{8–11} at XFELs, a technique that is well suited to room-temperature experiments and can overcome classical radiation dose limits by several orders of magnitude^{12,13}. By taking up to hundreds of thousands of snapshots of nano- to micrometer-sized crystals, SFX has been used to solve more than 80 biomolecular structures to date. The method has also been successfully extended to the time domain to investigate protein kinetics and enzyme reactions^{14,15}. SFX therefore not only has the potential to yield high-resolution information about the virus structure itself but also allows for investigation of dynamics, because many viral proteins undergo structural changes during their life cycles, for example as a result of protein interactions with cellular receptors and pH changes during entry through the endosome^{16–18}.

A continuing limiting factor for virus SFX in particular is efficient sample delivery, because typically only microgram amounts of virus crystals are available. Most SFX experiments today are carried out with gas dynamic virtual nozzles and high-viscosity gel matrices typically requiring more than 500 µg (~370 nL) of sample for structure determination^{19–26}.

In a first attempt of virus crystallography at XFELs²⁷, 10⁴ microcrystals of the Sindbis virus with an ~700 Å unit-cell dimension were suspended in a slow-moving stream of agarose and exposed to XFEL pulses. Through this approach, diffraction patterns were obtained with up to ~40-Å resolution and a 0.8% hit rate, defined as the percentage of images containing a certain number of Bragg spots. Owing to the technological challenges, especially

¹Photon Science, Deutsches Elektronen-Synchrotron DESY, Hamburg, Germany. ²Division of Structural Biology, Wellcome Trust Centre for Human Genetics, University of Oxford, Oxford, UK. ³Diamond Light Source Limited, Didcot, UK. ⁴Institute of Photonics, University of Eastern Finland, Joensuu, Finland. ⁵Molecular Biophysics and Integrated Bioimaging Division, Lawrence Berkeley National Laboratory, Berkeley, California, USA. ⁶School of Molecular and Cellular Biology, Faculty of Biological Sciences, University of Leeds, Leeds, UK. ⁷Pirbright Institute, Pirbright, UK. ⁸Linac Coherent Light Source, SLAC National Accelerator Laboratory, Menlo Park, California, USA. ⁹Paul Scherrer Institut, Villigen-PSI, Switzerland. ¹⁰Center for Free Electron Laser Science (CFEL), Hamburg, Germany. ¹¹These authors contributed equally to this work. Correspondence should be addressed to A.M. (alke.meents@desy.de).

the amount of sample required, to our knowledge, no previous virus structure has been determined at an XFEL.

A promising sample-delivery approach for SFX is the use of solid sample supports, also referred to as fixed targets^{28–37}, especially if the sample is limited. Here, several tens to thousands of crystals are loaded onto a structured solid support and are automatically raster-scanned during X-ray exposure. Major challenges for fixed-target experiments are the fast and precise scanning of these supports and the synchronization of predefined sample positions with the arrival of XFEL pulses.

Such experiments have been performed in step-scanning mode, which is less efficient than other sample-delivery methods, owing to the relatively long data collection times^{34,38}. Another obstacle for fixed-target experiments is the relatively high background scattering level, which is mainly caused by air scattering from the direct beam. Further contributions originate from scattering by nonsample material such as the surrounding mother liquor or the Kapton or Mylar foil typically used as a sealing material to prevent crystal dehydration.

Here, we report a method for fixed-target serial crystallography at low background levels and a sample exchange rate of 120 Hz, which requires only micrograms of sample. We demonstrate the applicability of our method for virus structure determination, shown for an intact virus, BEV2, and cytoplasmic polyhedrosis virus type 18 polyhedrin (CPV18).

BEV2 belongs to the virus family Picornaviridae, genus *Enterovirus*, and is a nonenveloped, positive-stranded RNA virus of 30 nm in diameter, which is endemic in cattle environments^{39–41}. Unlike some other picornaviruses, it is not a severe economic or animal-health threat and is therefore a suitable model system for the investigation of biological processes such as virus uncoating, which are universal to all enteroviruses. Enteroviruses (including BEV2) are stabilized by lipid cofactors such as sphingosine, which bind to a hydrophobic pocket of the VP1 capsid protein⁴². Potent binders to this pocket have potential as antivirals (by preventing uncoating); hence, we investigated the specificity of binding natural and synthetic moieties in this pocket. BEV2 crystals represent a challenging system for current SFX experiments, possessing a large unit-cell constant of 436.6 Å; moreover, typically only microgram quantities of small crystals are available.

Cytoplasmic polyhedrosis viruses (CPVs) are found as parasites in many insects and cause substantial losses in silkworm cocoon harvests⁴³. CPV strains have polyhedral crystals varying in size from hundreds of nanometers to several micrometers and contain several thousands of CPV particles^{43–46}, thus providing protection against environmental insults. CPV polyhedra were chosen as a well-established and robust model system for SFX data collection at cryogenic temperatures⁴⁷.

RESULTS

High-speed fixed-target structure-determination approach

Microcrystals of BEV2 and CPV18 were measured by fixed-target SFX with the Roadrunner goniometer installed at the XPP instrument at the LCLS (**Supplementary Fig. 1**). The Roadrunner setup consists of high-precision *x* and *y* piezomotor-driven scanning stages mounted on a horizontal translation stage and a vertical rotation axis (**Supplementary Fig. 2**; details in Online Methods). A high-magnification inline microscope allows for visualization of samples and their support structure (**Supplementary Fig. 3**).

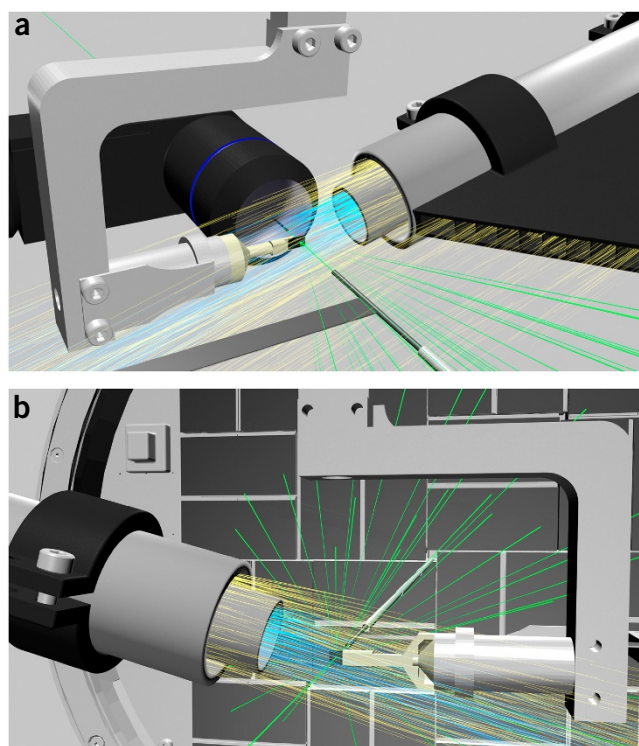


Figure 1 | Low-background experimental setup for fast fixed-target SFX experiments using the Roadrunner goniometer. **(a)** Front view. The silicon chip is raster-scanned through the X-ray beam (green) while being maintained under a continuous stream of humidified air (blue). A helium sheath flow (yellow) is used to confine the humidity stream and to decrease air scattering. Air scattering is further decreased by helium injection along the beam path. An inline microscope is used for proper chip alignment and definition of the scanning grid. **(b)** Back view. X-ray diffraction caused by the sample crystals is recorded with a Cornell-SLAC hybrid pixel array detector (CSPAD). After hitting the sample, the primary beam is enclosed by a molybdenum tubule and additional steel tubules, which further absorb air-scattered photons. In **b**, the inline microscope is omitted for clarity.

The Roadrunner setup is capable of data collection at both room temperature and cryogenic temperatures.

To decrease air scattering of X-rays, most of the path of the direct beam in air is enclosed in capillary shields, both upstream and downstream of the sample, thus decreasing the free path of the direct beam in air to 20 mm (**Supplementary Fig. 4**). By streaming helium gas across the remaining unenclosed direct beam behind the sample, the number of photons scattered by air is further decreased (**Fig. 1**). By combining these two approaches, air scattering can be decreased by a factor of ~8.

By use of micropatterned chips made of single-crystalline silicon as a substrate material, the background scattering signal caused by the support can be further decreased³¹. Dehydration of the crystals is prevented either by keeping them constantly under a stream of humidified gas^{32,48} or by flash freezing them and collecting data at cryogenic temperatures³¹ (**Supplementary Fig. 5**). With this approach, sealing of the sample holders, for example with Mylar foil, which would result in an increased background scattering level, is not required.

Our silicon chip (**Fig. 2a**) provides 22,500 pores for crystals³¹. For sample loading, 2–3 μ L of sample suspension is pipetted onto

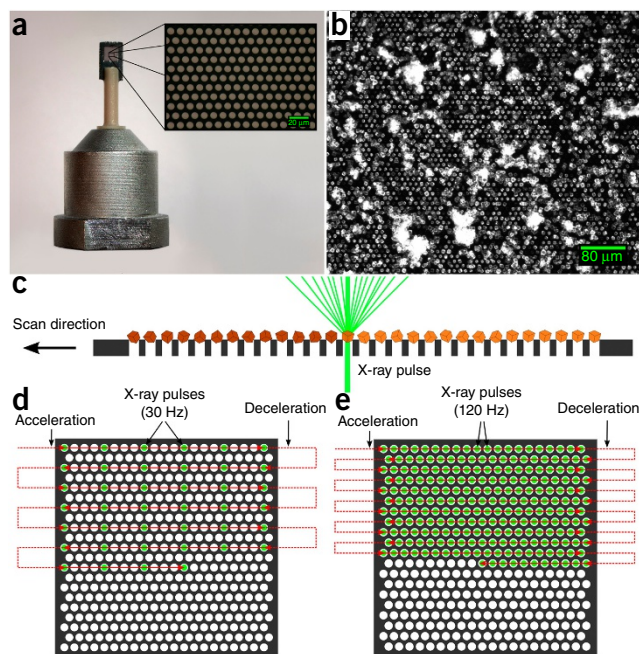


Figure 2 | Design of the micropatterned silicon chip and data collection strategy. (a) The chip is attached to a plastic rod for the purpose of thermal isolation. The membrane part within the outer frame consists of micropores with diameters of typically 4–8 μm , which are arranged in a triangular grid (inset). (b) The chip acts as a sample holder for more than 20,000 microcrystals, which largely organize themselves according to the pore pattern. (c) After loading, the microcrystals are scanned through the X-ray beam. By shooting the beam through the micropores in the chips, the interaction of the X-rays with any support material is further minimized. (d,e) Scanning strategies for measurements performed at room temperature (d) and cryogenic temperatures (e) (details in text).

the chip, so that the amount of sample material used is typically in the range of several micrograms, depending on the crystal sizes, the desired coverage of the chip membrane, and the amount of sample available^{31,32}. The resulting arrangement of the crystals is due to the pore pattern and allows for a highly efficient measurement strategy by shooting the free-electron laser (FEL) pulses through all pores in a fully automated procedure (Fig. 2b,c). With the Roadrunner control software, the scan points are defined by drawing a grid, which is graphically overlaid on the inline-microscope image (Supplementary Fig. 6). For data collection, the coordinates of scan points are downloaded to the motion controller, and the entire chip is scanned in a meander-scan manner (Fig. 2d,e; details in Online Methods). With this approach, most

of the crystalline material is used for the diffraction experiment and is not wasted.

To achieve fixed-target data collection rates of 120 Hz, we developed an improved version of the so-called fly scan. In a conventional fly scan, the sample is accelerated and then moved along a predefined trajectory at a constant velocity. This approach would in principle allow for data collection at 120 Hz, but in most cases it results in lower hit rates than those obtained with our method, because the X-ray pulses do not always hit through the pores where the crystals are located. To achieve higher hit rates—and thereby require substantially less sample—more precise motion control is required. Such an approach demands, in addition to velocity control, phase control of the movement of the stages with respect to the arrival of the X-ray pulses. The synchronized movement assures that every X-ray pulse hits through a pore (Fig. 2c–e, Online Methods and Supplementary Fig. 7).

BEV2 and CPV18 data collection

In the case of BEV2 samples, which were measured at room temperature, diffraction images were collected at an FEL pulse rate of 30 Hz per line, thus resulting in an effective frame rate of up to 12.2 images/s for each chip, when taking the time for line switching into account (Table 1 and Supplementary Table 1). A maximum hit rate of more than 9% for one chip and 5% on average was achieved for BEV2. The relatively low hit rates in this case were because the density of the crystals on the chip was low. Because only limited amounts of sample were available, we aimed at making the most efficient use of the available sample instead of optimizing hit rates. For room-temperature data collection, it was not possible to run at the full LCLS frame rate of 120 Hz, because crystals in the neighboring compartments were already predamaged by the wings of the X-ray beam. When shooting every fourth hole (40- μm separation) in the horizontal direction and every second row in the vertical direction (20- μm separation), we observed no effects of predamage (Fig. 2d). With a maximum speed of the horizontal scanning stage of 2.5 mm/s, data collection at 60 Hz with 40 μm separation or at 120 Hz with 20 μm separation would also have been possible.

For CPV18, data collection was performed at cryogenic temperatures with the full LCLS repetition rate of 120 Hz, thus resulting in an average data collection rate of 33.6 images/s (Fig. 2e). From these images, more than 70% were classified as hits. In other runs, we were able to achieve hit rates of more than 90%. No predamage of the neighboring crystals by the wings of the X-ray beam was observed for CPV18, probably because of decreased diffusion rates of free radicals and the resulting higher radiation tolerance of macromolecular crystals at cryogenic temperatures^{5–7}.

Table 1 | Data collection parameters and hit rates for individual runs

Run number	Sample	Temperature Conditions	Number of images	Acquisition time (s)	Effective acquisition rate (images/s)	Number of hits ^a	Hit rate (%)	Indexed
294	BEV2	293 K	2,280	230.7	9.9	159	7.0	124
296	BEV2	293 K	180	14.8	12.2	17	9.4	16
298	BEV2	293 K	1,950	178.0	11.0	76	3.9	69
301	BEV2	293 K	2,015	180.7	11.2	150	7.4	113
303	BEV2	293 K	2,387	214.4	11.1	44	1.8	30
47	CPV18	100 K	19,028	566.1	33.6	13,424	70.5	16,739

^aImages containing ≥ 50 (BEV2) and 20 (CPV18) strong spots were considered hits. Spot-finding parameters can be found in Supplementary Table 1.

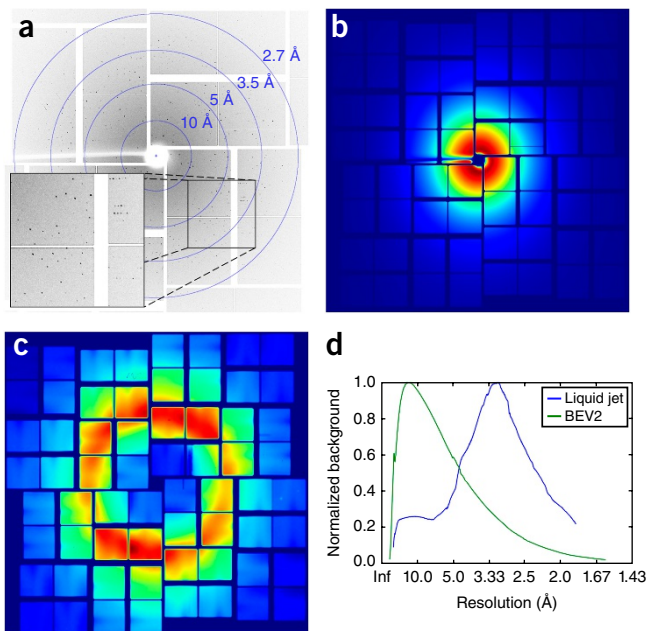


Figure 3 | Exemplary BEV2 diffraction pattern and comparison of background scattering levels achievable with different sample-delivery methods. **(a)** Diffraction image of BEV2 microcrystals obtained at the XPP instrument at LCLS by using the micropatterned silicon chip as a sample holder. **(b)** Owing to the efficient removal of successive mother liquor during sample loading, no water ring is observed in the averaged background image of the chip. **(c)** Averaged background image from a typical SFX liquid jet experiment with CPV17 crystals⁴⁷, shown for comparison. Inf, infinite. **(d)** The azimuthally averaged radial distribution of both images is plotted as a function of resolution. Both curves are normalized because measurements were performed under different experimental conditions, and therefore a direct comparison was not possible.

Image quality and background analysis

The diffraction patterns extended to a resolution of 2.3 Å for BEV2 and 2.4 Å for CPV18. An example diffraction image (**Fig. 3a**) obtained from a BEV2 crystal illustrates the high quality of the diffraction patterns obtained with the Roadrunner goniometer. The low background contribution of the chip resulted in high-resolution diffraction data with high signal-to-noise ratios. We analyzed the averaged background signal of the measured diffraction images (**Fig. 3b**) and compared it with that from an SFX experiment in which a liquid jet was used for sample delivery (**Fig. 3c**). The azimuthally averaged background signal as a function of resolution clearly showed that in the diffraction images measured with our fixed-target setup, the background was dominated by air scattering, which was most prominent at resolutions below 10 Å (**Fig. 3d**). The chip itself consisted of single-crystalline silicon and therefore did not contribute to any background signal. The absence of a water ring for room-temperature data collection revealed the efficient removal of mother liquor during sample loading. In typical liquid jet experiments, the averaged background signal showed a strong water ring around 3.1 Å.

Structure determination

Summary information regarding data collection and structure refinement for both samples is given in **Supplementary Table 2** (PDB 5MQU for BEV2 and PDB 5MQW for CPV18). The structure

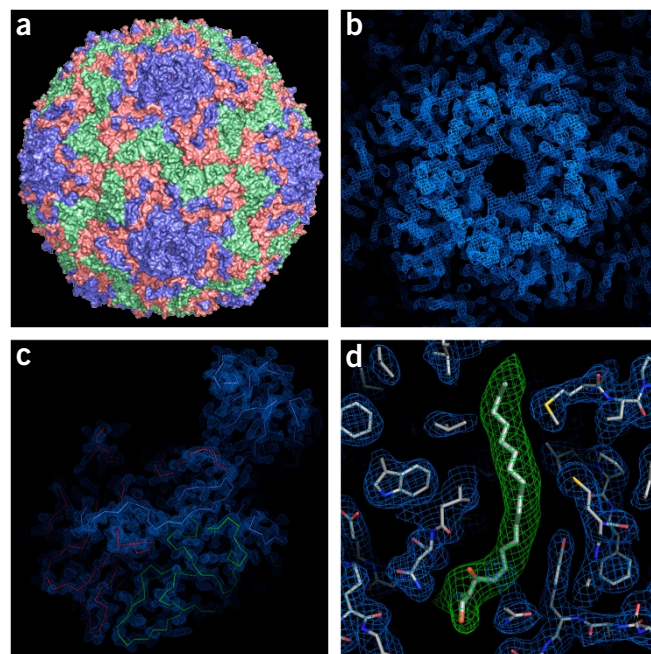


Figure 4 | Overall structure of BEV2 and corresponding high-resolution electron density maps. **(a)** Surface representation of the BEV2 particle, as viewed toward an icosahedral two-fold axis. VP1, VP2, and VP3 are shown in blue, green, and red, respectively. **(b,c)** Electron density maps after one cycle of five-fold real-space averaging by using the phases calculated from the current refined model showing the electron density around the five-fold axis in **b** and for a biological protomer in **c**. **(c)** Coarse traces of VP1–3, colored as in **a**. **(d)** A close-up view of the electron density for protein residues around the pocket-factor-binding site of VP1 (blue mesh and thinner sticks) and density for the pocket factor (thicker sticks show a sphingosine fitted to the density, and the green density is for a simulated annealing omit map).

of BEV2 was solved by using diffraction data obtained from five chips, from a total of ~446 crystal hits in less than 14 min of scanning time. For CPV18, the complete structure was able to be solved with the data obtained from only a single chip, collected in less than 10 min. Unfortunately, the resolution was limited by the dimensions of the detector for the given detector distance in that case. Structure refinement (on the basis of prior models) yielded high-quality electron density maps (**Fig. 4**) with model R values of $R_{\text{work}}/R_{\text{free}} = 23.3/25.7\%$ for BEV2 (to 2.3-Å resolution; data were measurable to 2.0-Å resolution, but the resulting map was only marginally improved, and the statistics were significantly worse) and 11.3/14.5% for CPV18 (to 2.4-Å resolution).

The CPV18 data were measured with high redundancy (>100-fold) and were of very high quality ($R_{\text{split}} 9.2\%$, $CC_{1/2} 0.993$), thus supporting the excellent refinement. In contrast, the BEV2 data were derived from only 324 crystals and had a multiplicity of only 2, and the merging statistics were correspondingly poor ($R_{\text{split}} 48.6\%$, $CC_{1/2} 0.746$). We therefore performed two tests to determine whether the amplitudes contained sufficient information to determine the high-resolution structure in the absence of accurate phase information. First, we extended the phases by using five-fold noncrystallographic symmetry (NCS) averaging and solvent flattening from 5-Å to 2.5-Å resolution. The result was an excellent map with largely successful phase

recovery (details in Online Methods and **Supplementary Fig. 8**). Second, we performed molecular replacement starting from a distantly related virus (FMDV type A22, sequence identity 19.5%). As expected, the initial map showed substantial bias; however, this bias was eliminated by cyclic averaging, thus again resulting in a high-quality electron density map (Online Methods and **Supplementary Figs. 9 and 10**).

The BEV2 structure was determined as part of an investigation of the specificity of the hydrophobic pocket in VP1 for different fatty acids. The structure revealed that despite the cocrystallization of the virus with lauric acid, the pocket factor present in the particles was indistinguishable from that observed in native particles and was well modeled as sphingosine (**Fig. 4d**), thus explaining the biophysical observations that lauric acid has essentially no effect on the stability of the virus particles.

The CPV18 structure is similar to recently published structures of isolated crystals of CPV18 (refs. 31,49). A part of the electron density map is shown in **Supplementary Figures 11 and 12**.

DISCUSSION

To our knowledge, this report describes the first structure of a virus particle determined at an XFEL by means of serial crystallography. The electron density maps obtained for BEV2 provide a high level of detail sufficient to demonstrate that lauric acid cannot displace sphingosine from the VP1 pocket, which is the major target for the design of antienteroviral compounds. We further showed that the method is also applicable to data collection at cryogenic temperatures, at which hit rates of more than 70% were achieved, and the structure of CPV18 crystals was solved from the measurement of one chip loaded with ~4 µg of protein.

The periodic arrangement of the crystals on our chip in combination with the Roadrunner goniometer allows for very effective use of beam time. With data collection rates of 120 Hz during a line scan, combined with hit rates of more than 70%, we were able to obtain up to 29.6 indexable diffraction patterns per second. Sample loading onto the chip is very efficient, and no precious crystalline material is lost. The method is probably more reliable than liquid jet experiments, which often have drawbacks such as nozzle clogging and crystal settling, which lead to substantial downtime during the experiments.

A further benefit of our method is its ultralow sample consumption, which requires orders of magnitude less sample than that required in current liquid jet methods at XFELs and room-temperature experiments at synchrotrons. A synchrotron structure⁴ of the apo form of the BEV2 capsid has previously been determined at 2.1-Å resolution, on the basis of the measurement of 28 crystals of a cubic edge length of ~50 µm, thus amounting to a total crystal volume of 3.5 nL. Our work was based on data collected from 446 much smaller crystals with a cubic edge length of only ~8 µm, corresponding to a total volume of 228 pL. Cocrystallization of BEV2 with lauric acid limits the achievable crystal size and renders these crystals far too small for conventional synchrotron structure determination. The use of the XFEL therefore not only provided the high intensity X-ray pulses required to generate sufficiently strong diffraction to solve the ligand-bound virus structure but also decreased the total sample amount used for structure-factor calculation by 15-fold. Notably, high-quality phases and hence electron density maps were able to be derived from amplitudes assembled from such little material

and such a low-multiplicity XFEL data set assembled from only 324 crystals. We attribute this ability to the high quality of the data obtained from this experimental setup, to advances in data processing methods, and in part to the five-fold noncrystallographic symmetry.

In the current setup, the X-ray-scattering background is dominated by air scattering from the short remaining beam path in humidified air or cold nitrogen gas. By further decreasing the path of the primary beam in air and by replacing air or nitrogen with helium, we aim to significantly decrease the background level in future experiments to achieve higher-resolution data from even smaller crystals. A larger chip design with up to 200,000 micropores in combination with faster scanning stages would allow for longer data collection runs at frame rates of up to 1 kHz, thereby resulting in even more efficient use of beam time at both XFELs and synchrotron facilities.

METHODS

Methods, including statements of data availability and any associated accession codes and references, are available in the [online version of the paper](#).

Note: Any Supplementary Information and Source Data files are available in the online version of the paper.

ACKNOWLEDGMENTS

We thank the LCLS staff for their support during experiment LH90. Use of the LCLS, SLAC National Accelerator Laboratory, is supported by the US Department of Energy, Office of Science, Office of Basic Energy Sciences under contract no. DE-AC02-76SF00515. This work was further supported by the European Cluster of Advanced Laser Light Sources (EUCALL) and the Virtual Institute VH-VI-403 of the Helmholtz Association. H.M.G. was supported by the Wellcome Trust (studentship 075491/04). D.I.S. was supported by the Medical Research Council, grant MR/N00065X/1 and previously by G1000099. N.K.S. was supported by the US National Institutes of Health grants GM102520 and GM117126 for data processing methods. We further thank J. Bergtholdt from DESY for preparation of the technical drawings of the Roadrunner setup.

AUTHOR CONTRIBUTIONS

P.R., T.P., P.F., J.M., A.W., and A.M. designed the experiment. P.R., G.S., K.H., T.S.W., R.D., I.V., M.W., A.K., J.K., and D.J.R. were involved in sample preparation. P.R., T.P., G.S., K.H., J.M., P.F., R.D., B.R., M.S., S.N., D.S.D., R.A.-M., C.D., A.W., and A.M. participated in data collection. P.R., H.M.G., A.S.B., I.D.Y., T.M.-C., N.K.S., J.R., E.E.F., and D.I.S. analyzed the data. P.R., H.M.G., D.I.S., A.W., and A.M. wrote the manuscript.

COMPETING FINANCIAL INTERESTS

The authors declare competing financial interests: details are available in the [online version of the paper](#).

Reprints and permissions information is available online at <http://www.nature.com/reprints/index.html>. Publisher's note: Springer Nature remains neutral with regard to jurisdictional claims in published maps and institutional affiliations.

1. Zocher, G. *et al.* A sialic acid binding site in a human picornavirus. *PLoS Pathog.* **10**, e1004401 (2014).
2. Fry, E.E., Abrescia, N.G.A. & Stuart, D.I. in *Macromolecular Crystallography: Conventional and High-Throughput Methods* (eds. Sanderson, M.R. & Skelly, J.V.), 245–264 (Oxford, 2007).
3. Fry, E.E., Grimes, J. & Stuart, D.I. Virus crystallography. *Mol. Biotechnol.* **12**, 13–23 (1999).
4. Axford, D. *et al.* In situ macromolecular crystallography using microbeams. *Acta Crystallogr. D Biol. Crystallogr.* **68**, 592–600 (2012).
5. Hope, H. Cryocrystallography of biological macromolecules: a generally applicable method. *Acta Crystallogr. B* **44**, 22–26 (1988).
6. Owen, R.L., Rudiño-Piñera, E. & Garman, E.F. Experimental determination of the radiation dose limit for cryocooled protein crystals. *Proc. Natl. Acad. Sci. USA* **103**, 4912–4917 (2006).

7. Meents, A., Gutmann, S., Wagner, A. & Schulze-Bries, C. Origin and temperature dependence of radiation damage in biological samples at cryogenic temperatures. *Proc. Natl. Acad. Sci. USA* **107**, 1094–1099 (2010).
8. Chapman, H.N. *et al.* Femtosecond X-ray protein nanocrystallography. *Nature* **470**, 73–77 (2011).
9. Boutet, S. *et al.* High-resolution protein structure determination by serial femtosecond crystallography. *Science* **337**, 362–364 (2012).
10. Redecke, L. *et al.* Natively inhibited *Trypanosoma brucei* cathepsin B structure determined by using an X-ray laser. *Science* **339**, 227–230 (2013).
11. Ayyer, K. *et al.* Macromolecular diffractive imaging using imperfect crystals. *Nature* **530**, 202–206 (2016).
12. Neutze, R., Wouts, R., van der Spoel, D., Weckert, E. & Hajdu, J. Potential for biomolecular imaging with femtosecond X-ray pulses. *Nature* **406**, 752–757 (2000).
13. Barty, A. *et al.* Self-terminating diffraction gates femtosecond X-ray nanocrystallography measurements. *Nat. Photonics* **6**, 35–40 (2012).
14. Kupitz, C. *et al.* Serial time-resolved crystallography of photosystem II using a femtosecond X-ray laser. *Nature* **513**, 261–265 (2014).
15. Tenboer, J. *et al.* Time-resolved serial crystallography captures high-resolution intermediates of photoactive yellow protein. *Science* **346**, 1242–1246 (2014).
16. Perera, R., Khaliq, M. & Kuhn, R.J. Closing the door on flaviviruses: entry as a target for antiviral drug design. *Antiviral Res.* **80**, 11–22 (2008).
17. Connolly, S.A., Jackson, J.O., Jardetzky, T.S. & Longnecker, R. Fusing structure and function: a structural view of the herpesvirus entry machinery. *Nat. Rev. Microbiol.* **9**, 369–381 (2011).
18. Harrison, J.S. *et al.* Role of electrostatic repulsion in controlling pH-dependent conformational changes of viral fusion proteins. *Structure* **21**, 1085–1096 (2013).
19. Weierstall, U. *et al.* Lipidic cubic phase injector facilitates membrane protein serial femtosecond crystallography. *Nat. Commun.* **5**, 3309 (2014).
20. DePonte, D.P. *et al.* Gas dynamic virtual nozzle for generation of microscopic droplet streams. *J. Phys. D Appl. Phys.* **41**, 195505 (2008).
21. Caffrey, M. & Cherezov, V. Crystallizing membrane proteins using lipidic mesophases. *Nat. Protoc.* **4**, 706–731 (2009).
22. Liu, W. *et al.* Serial femtosecond crystallography of G protein-coupled receptors. *Science* **342**, 1521–1524 (2013).
23. Fromme, R. *et al.* Serial femtosecond crystallography of soluble proteins in lipidic cubic phase. *IUCr J* **2**, 545–551 (2015).
24. Sugahara, M. *et al.* Grease matrix as a versatile carrier of proteins for serial crystallography. *Nat. Methods* **12**, 61–63 (2015).
25. Sugahara, M. *et al.* Oil-free hyaluronic acid matrix for serial femtosecond crystallography. *Sci. Rep.* **6**, 24484 (2016).
26. Conrad, C.E. *et al.* A novel inert crystal delivery medium for serial femtosecond crystallography. *IUCr J* **2**, 421–430 (2015).
27. Lawrence, R.M. *et al.* Serial femtosecond X-ray diffraction of enveloped virus microcrystals. *Struct. Dyn.* **2**, 041720 (2015).
28. Zarrine-Afsar, A. *et al.* Crystallography on a chip. *Acta Crystallogr. D Biol. Crystallogr.* **68**, 321–323 (2012).
29. Hunter, M.S. *et al.* Fixed-target protein serial microcrystallography with an x-ray free electron laser. *Sci. Rep.* **4**, 6026 (2014).
30. Mueller, C. *et al.* Fixed target matrix for femtosecond time-resolved and in situ serial micro-crystallography. *Struct. Dyn.* **2**, 054302 (2015).
31. Roedig, P. *et al.* A micro-patterned silicon chip as sample holder for macromolecular crystallography experiments with minimal background scattering. *Sci. Rep.* **5**, 10451 (2015).
32. Roedig, P. *et al.* Room-temperature macromolecular crystallography using a micro-patterned silicon chip with minimal background scattering. *J. Appl. Cryst.* **49**, 968–975 (2016).
33. Oghbaei, S. *et al.* Fixed target combined with spectral mapping: approaching 100% hit rates for serial crystallography. *Acta Crystallogr. D Struct. Biol.* **72**, 944–955 (2016).
34. Cohen, A.E. *et al.* Goniometer-based femtosecond crystallography with X-ray free electron lasers. *Proc. Natl. Acad. Sci. USA* **111**, 17122–17127 (2014).
35. Murray, T.D. *et al.* A high-transparency, micro-patternable chip for X-ray diffraction analysis of microcrystals under native growth conditions. *Acta Crystallogr. D Biol. Crystallogr.* **71**, 1987–1997 (2015).
36. Baxter, E.L. *et al.* High-density grids for efficient data collection from multiple crystals. *Acta Crystallogr. D Struct. Biol.* **72**, 2–11 (2016).
37. Owen, R.L. *et al.* Low-dose fixed-target serial synchrotron crystallography. *Acta Crystallogr. D Struct. Biol.* **73**, 373–378 (2017).
38. Sherrell, D.A. *et al.* A modular and compact portable mini-endstation for high-precision, high-speed fixed target serial crystallography at FEL and synchrotron sources. *J. Synchrotron Radiat.* **22**, 1372–1378 (2015).
39. Smyth, M. *et al.* Preliminary crystallographic analysis of bovine enterovirus. *J. Mol. Biol.* **231**, 930–932 (1993).
40. Smyth, M. *et al.* Implications for viral uncoating from the structure of bovine enterovirus. *Nat. Struct. Biol.* **2**, 224–231 (1995).
41. Goens, S.D., Botero, S., Zemla, A., Zhou, C.E. & Perdue, M.L. Bovine enterovirus 2: complete genomic sequence and molecular modelling of a reference strain and a wild-type isolate from endemically infected US cattle. *J. Gen. Virol.* **85**, 3195–3203 (2004).
42. Filman, D.J. *et al.* Structural factors that control conformational transitions and serotype specificity in type 3 poliovirus. *EMBO J.* **8**, 1567–1579 (1989).
43. Coulbaly, F. *et al.* The molecular organization of cypovirus polyhedra. *Nature* **446**, 97–101 (2007).
44. Ji, X. *et al.* How baculovirus polyhedra fit square pegs into round holes to robustly package viruses. *EMBO J.* **29**, 505–514 (2010).
45. Anduleit, K. *et al.* Crystal lattice as biological phenotype for insect viruses. *Protein Sci.* **14**, 2741–2743 (2005).
46. Ji, X. *et al.* Polyhedra structures and the evolution of the insect viruses. *J. Struct. Biol.* **192**, 88–99 (2015).
47. Ginn, H.M. *et al.* Structure of CPV17 polyhedrin determined by the improved analysis of serial femtosecond crystallographic data. *Nat. Commun.* **6**, 6435 (2015).
48. Sanchez-Weatherby, J. *et al.* Improving diffraction by humidity control: a novel device compatible with X-ray beamlines. *Acta Crystallogr. D Biol. Crystallogr.* **65**, 1237–1246 (2009).
49. Axford, D., Ji, X., Stuart, D.I. & Sutton, G. In cellulo structure determination of a novel cypovirus polyhedrin. *Acta Crystallogr. D Biol. Crystallogr.* **70**, 1435–1441 (2014).

ONLINE METHODS

A detailed step-by-step protocol of our method is provided as a **Supplementary Protocol** and is also available on the Protocol Exchange from Nature Protocols⁵⁰.

Sample preparation. Bovine enterovirus 2 light fraction (BEV2) was prepared at the Department of Microbiology, University of Leeds, UK, by the group of D.J.R. Particles were purified by ultracentrifugation over a 30% sucrose cushion followed by a 15–45% sucrose gradient. Fractions containing BEV2 particles were pooled, incubated with lauric acid, and pelleted by ultracentrifugation by J.K. To remove excess lauric acid, particles were solubilized in 20 mM HEPES, pH 8.0, 200 mM NaCl, and 0.5% NP-40 at 4 °C, and pelleted again by ultracentrifugation with a 30% sucrose cushion. The pellet was solubilized in 20 mM HEPES, pH 8.0, and 200 mM NaCl. Crystals were grown from the purified concentrated particles by vapor diffusion in Greiner ‘CrystalQuick X’ plates at 293 K. Drops of 100 nL of BEV2 particles ($A_{280} = 5$) were mixed with 100-nL drops⁵¹ of the precipitant (1.5 M ammonium sulfate and 0.1 M Tris, pH 8) and equilibrated against 35 μ L of precipitant. More than 100 small crystals, with typical dimensions of $8 \times 8 \times 8 \mu\text{m}^3$, appeared in each drop within hours. An image of the BEV2 crystals is shown in **Supplementary Figure 13**. CPV18 polyhedrin crystals were prepared as described previously³¹.

Chip design and fabrication. The chip design is illustrated in **Figure 2**. The chips were made from single-crystalline silicon by UV lithography and had overall dimensions of $2.5 \times 4 \text{ mm}^2$ with a thickness of 0.1 mm. The inner-membrane part with an area of $1.5 \times 1.5 \text{ mm}^2$ was thinned down to a thickness of 10 μm and provided a hexagonal dense pattern of pores with diameters between 4 μm and 8 μm and a 10- μm periodicity (**Fig. 2a**). The chips were glued to plastic pins, which could be mounted on conventional magnetic caps routinely used in macromolecular crystallography. More details about chip design, fabrication, loading, and handling can be found in ref. 31.

Preorientation of the chips. With the extremely high X-ray intensity per FEL pulse, Bragg reflections arising from the silicon chip material can easily damage the detector. Hence, it is essential to know the exact angular orientation of the chips with respect to the incident X-ray beam to avoid these Bragg reflections. As a reference mark, the magnetic caps carrying the chips were modified by removing some material at the lower rim of the caps, as shown in **Figure 2a**. All chips glued to the plastic pins were then oriented and fixed such that the chip surface was always parallel to the face of the magnetic caps.

Sample loading. Sample loading was performed by applying 2–3 μL of crystal suspension to the upper side of the chip. Additional mother liquor was then removed by soaking with a wedge of filter paper attached to the lower side of the chip (details in ref. 31). The chip allowed for data collection at both room temperature (BEV2) and cryogenic temperatures (CPV18). For room-temperature data collection, the samples were loaded onto the chips directly at the experimental setup. Similarly to recently performed synchrotron experiments³², a humidified gas stream with adjustable relative humidity was used to prevent the crystals from drying out during loading and data collection^{48,52}. For BEV2 data collection, the

relative humidity was set to 96%. The experimental setup could be also used for data collection at cryogenic temperatures. The major difference was simply the replacement of the humidity stream used for room-temperature data collection by a cold nitrogen-gas stream. In that case, prefrozen samples on the chips were directly mounted on the goniometer.

Roadrunner goniometer. For the experiment, we designed a special goniometer whose main part was a fast piezomotor-driven x,y translation stage for fast raster-scanning of the chips carrying the samples. A technical overview drawing of the Roadrunner goniometer is provided in **Supplementary Figure 1**. The setup consisted of three major components—a high-resolution inline sample-viewing microscope, the high-precision goniometer itself, and a post sample beam pipe unit—all mounted on a common support frame structure. With outer dimensions of 250 mm along the beam direction, a width of 400 mm and a height of 515 mm, the entire setup is compact and could be therefore easily installed at different experimental endstations such as XPP (as presented here), the new MFX endstation at LCLS, or other X-ray sources.

The first element in the X-ray beam path, the inline sample-viewing microscope, is shown and described in more detail in **Supplementary Figure 3**. The microscope provides a high-resolution image of the samples mounted on the goniometer and is used for precise alignment of the chips with respect to the X-ray beam. The X-ray beam passes through a molybdenum collimator tube inserted into the hole of the objective lens with an inner diameter of 0.35 mm. The capillary is used to prevent X-ray damage to the microscope lenses, and it extends to only 3 mm from the sample position to decrease air scattering along the beam path.

The micropatterned silicon chip carrying the samples is mounted on a high-precision goniometer axis. A technical drawing of the goniometer and a detailed description of its functionality are provided in **Supplementary Figure 2**. The main element is the high x,y precision stage for scanning of the chips synchronized to the time structure of the X-ray pulses. The x,y scanning stage was controlled by a DMC-4080 motion controller from Galil. The motion controller was capable of synchronizing the two axes of the scanning stage to the repetition rate of the LCLS beam at 120 Hz. The synchronization was done on a line-by-line basis to ensure that each X-ray pulse hit the center of the holes in the silicon chip. For each line, the motion controller was provided with the starting point, the number of scan points (number of holes), the angular orientation of the line, and the repetition rate of the LCLS beam. The synchronization scheme is illustrated and described in more detail in **Supplementary Figure 7**. After the start, the controller moves the scanning stages to a defined position before the first scan point and sends a trigger signal to the LCLS control system. This trigger signal induces a defined sequence of TTL signals to be sent from the LCLS control system to the motion controller, to allow the scanning stage to reach a constant speed and the position of the chip pores to be in phase with the arrival of the X-ray pulses at the predefined beam position. After the starting point of the grid is reached, the pulse picker opens, and the X-rays hit the crystals located in the pores of the chip. At each scan point, the current position is read out by the controller, and any error is instantaneously injected into the control loop and compensated for to prevent accumulation of errors. After a predefined number of pulses (equal to the number

of pores selected) has been reached, the pulse picker closes, and the scanner decelerates before switching to the next line of the chip. This sequence is repeated for all rows of the chip in a meander-scan-like manner.

After interacting with the sample, the direct undiffracted beam is guided into a beam pipe, which is shown and described in **Supplementary Figure 4**. By enclosing the beam in a beam pipe, all X-rays scattered by air are absorbed in the walls of the tube and thereby do not contribute to background scattering at the detector.

Roadrunner control system and software. Alignment of the goniometer setup, control of individual motors, prealignment of the individual chips, definition of the scan grid, and data collection are controlled by custom software written in the Python programming language with the underlying control system TANGO. The software provides a graphical user interface (GUI) for easy and efficient operation. A screenshot of the Roadrunner GUI together with a more detailed functionality of the software is provided in **Supplementary Figure 6**. The style and functionality of the GUI were adapted from GUIs typically used at protein crystallography beamlines. The software is available for free download at <http://doi.org/10.5281/zenodo.571598>.

Data collection. Measurements were conducted on the XPP instrument at the LCLS at SLAC under experiment number LH90. An X-ray energy of 9.5 keV was chosen for the experiment because it provides a good compromise between detector efficiency and pulse intensity on the one hand and X-ray absorption by the silicon chips on the other hand. The X-ray beam size at the sample was $3 \times 3 \mu\text{m}^2$. X-ray pulse energies were attenuated to 40% of the full flux. A photograph of the Roadrunner setup installed at the XPP instrument at LCLS is shown in **Supplementary Figure 5**.

For measurements performed at room temperature, it was observed that, with the aforementioned procedure, only the first shot of each line yielded useful diffraction data, probably because of predamage of the subsequent crystals by the wings of the X-ray beam. It was therefore necessary to increase the displacement of subsequent pulses to prevent damage of the crystals caused by the previous X-ray pulse. For this reason, the beam shutter was used to chop the repetition rate of the laser to 30 Hz, shooting only every fourth hole in the chip (**Fig. 2d**). In addition, during the scan, only every second line of the chip membrane was scanned. In this way, an effective acquisition rate of up to 12.2 images/s was achieved for room-temperature measurements.

At cryogenic temperatures in each line, the chip was translated with a speed of 1.2 mm/s, so that the displacement of subsequent pulses matched the distance between two neighboring holes in the chip (**Fig. 2e**). Thus, a maximum data acquisition rate of 120 Hz could be achieved within a line. After the end of a line was reached, the chip moved to the next line and scanned in the reverse direction. This process allowed for scanning of the entire chip membrane with ~19,000 collected detector frames in less than 10 min, thus resulting in an effective data acquisition rate of 33.6 images/s (**Table 1**).

Data evaluation and structure refinement. Diffraction images considered hits were isolated from the XTC streams with *cctbx.xfel*

and were passed into the data processing pipeline *cpxxfel*⁵³. Technical difficulties with indexing the BEV2 diffraction patterns drove the development of a new indexing algorithm called TakeTwo⁵⁴. Owing to the increased indexing rate from this algorithm, the TakeTwo algorithm was used to index both the BEV2 and CPV18 samples. Integration, initial orientation matrix refinement, and postrefinement were carried out similarly to previously described procedures^{47,53}. Geometry was refined initially with *cctbx.xfel* and then was further refined with the geometry algorithm in *cpxxfel* by using the spot predictions from the indexing solutions and the nearest peak pixel value. For BEV2, a 2×2 foreground integration window was used to match the spot size, and care was taken to ensure that the background subtraction region did not overlap with a neighboring spot. After geometry refinement, the accuracy of spot prediction allowed interpolation between pixels to be used. After postrefinement, the BEV2 data were reintegrated with the updated orientation matrix to more accurately predict the spot positions. For CPV18, the integration window was 5×5 , owing to the larger spot size.

For the BEV2 samples, 446 detector frames out of 8,812 collected images from five different chips were classified as possible hits (**Table 1**). Among these, 352 indexed diffraction patterns were obtained, of which 324 diffraction patterns were included in the final data set and used for structure refinement. To test whether the amplitudes were sufficiently accurate and complete to support phase determination, an initial map was calculated from phase information by using the known BEV coordinates truncated to 5 Å. Density modification, NCS averaging and gradual phase extension was performed from 5 Å to 2.5 Å, thus providing a good interpretable map with clear side chain density (**Supplementary Fig. 8**, which also shows the relationship between the phases derived from phase extension and those derived from an averaged map obtained from the synchrotron data). The atomic coordinates were rebuilt into the map derived from phase extension to remove bias from the model reported by Axford *et al.*⁴, by using CNS⁵⁵ with strict NCS constraints. The resulting BEV2 electron densities are shown in **Figure 4**. In a second test, phases derived from the suitably placed capsid of FMDV A22 were combined with amplitudes from BEV2 (to a resolution of 2.3 Å). The level of sequence identity between the capsid protein of these two viruses was only 19.5%. This map was then refined by cyclic density modification and NCS averaging (**Supplementary Figs. 9 and 10**).

For the CPV18 sample, 13,424 diffraction images out of 19,028 collected images were regarded as hits, all from one single chip. Images were indexed with the multiple lattice version of the TakeTwo algorithm, thus producing 16,739 indexing solutions. Up to five diffraction patterns could be indexed on a single image, owing to multiple hits (**Supplementary Fig. 14**). Finally, 9,293 patterns were included in the final data set. For structure refinement of CPV18, phases were introduced from PDB 4OTS as a template file, and the structure was refined with Phenix⁵⁶. Further data evaluation details are summarized in **Supplementary Table 2**. Part of the electron density map for CPV18 is shown in **Supplementary Figures 10 and 11**.

Statistics. Statistical measures addressing the quality of the two refined structures are provided in **Supplementary Table 2**.

Code availability. The Roadrunner control software is available under doi 10.5281/zenodo.571598 (<http://doi.org/10.5281/zenodo.571598>).

Data availability. Solved structures have been deposited in the Protein Data Bank under PDB 5MQU and PDB 5MQW for BEV2 and CPV18, respectively. Source data for **Figure 3d** are provided as a separate data file.

50. Roedig, P. *et al.* Sample preparation and data collection for high-speed fixed-target serial femtosecond crystallography. *Protocol Exchange* <http://dx.doi.org/10.1038/protex.2017.059> (2017).
51. Walter, T.S. *et al.* A procedure for setting up high-throughput nanolitre crystallization experiments: crystallization workflow for initial screening, automated storage, imaging and optimization. *Acta Crystallogr. D Biol. Crystallogr.* **61**, 651–657 (2005).
52. Wheeler, M.J., Russi, S., Bowler, M.G. & Bowler, M.W. Measurement of the equilibrium relative humidity for common precipitant concentrations: facilitating controlled dehydration experiments. *Acta Crystallogr. F Struct. Biol. Cryst. Commun.* **68**, 111–114 (2012).
53. Ginn, H.M., Evans, G., Sauter, N.K. & Stuart, D.I. On the release of *cpxfel* for processing X-ray free-electron laser images. *J. Appl. Crystallogr.* **49**, 1065–1072 (2016).
54. Ginn, H.M. *et al.* TakeTwo: an indexing algorithm suited to still images with known crystal parameters. *Acta Crystallogr. D Struct. Biol.* **72**, 956–965 (2016).
55. Brunger, A.T. Version 1.2 of the Crystallography and NMR system. *Nat. Protoc.* **2**, 2728–2733 (2007).
56. Adams, P.D. *et al.* PHENIX: a comprehensive Python-based system for macromolecular structure solution. *Acta Crystallogr. D Biol. Crystallogr.* **66**, 213–221 (2010).